

Zeitschrift:	Schweizerische mineralogische und petrographische Mitteilungen = Bulletin suisse de minéralogie et pétrographie
Band:	81 (2001)
Heft:	2
Artikel:	The kinematics of the Southern Passeier fault : radiometric and petrographic constraints
Autor:	Spiess, Richard / Marini, Matteo / Frank, Wolfgang
DOI:	https://doi.org/10.5169/seals-61688

Nutzungsbedingungen

Die ETH-Bibliothek ist die Anbieterin der digitalisierten Zeitschriften auf E-Periodica. Sie besitzt keine Urheberrechte an den Zeitschriften und ist nicht verantwortlich für deren Inhalte. Die Rechte liegen in der Regel bei den Herausgebern beziehungsweise den externen Rechteinhabern. Das Veröffentlichen von Bildern in Print- und Online-Publikationen sowie auf Social Media-Kanälen oder Webseiten ist nur mit vorheriger Genehmigung der Rechteinhaber erlaubt. [Mehr erfahren](#)

Conditions d'utilisation

L'ETH Library est le fournisseur des revues numérisées. Elle ne détient aucun droit d'auteur sur les revues et n'est pas responsable de leur contenu. En règle générale, les droits sont détenus par les éditeurs ou les détenteurs de droits externes. La reproduction d'images dans des publications imprimées ou en ligne ainsi que sur des canaux de médias sociaux ou des sites web n'est autorisée qu'avec l'accord préalable des détenteurs des droits. [En savoir plus](#)

Terms of use

The ETH Library is the provider of the digitised journals. It does not own any copyrights to the journals and is not responsible for their content. The rights usually lie with the publishers or the external rights holders. Publishing images in print and online publications, as well as on social media channels or websites, is only permitted with the prior consent of the rights holders. [Find out more](#)

Download PDF: 09.08.2025

ETH-Bibliothek Zürich, E-Periodica, <https://www.e-periodica.ch>

The kinematics of the Southern Passeeier fault: radiometric and petrographic constraints

by Richard Spiess^{1,2}, Matteo Marini¹, Wolfgang Frank³, Bruno Marcolongo⁴
and Giancarlo Cavazzini²

Abstract

The 20 km long Southern Passeeier fault has been recognised to the SSW of Meran (Northern Italy, Eastern Alps). The existence of this fault is shown by satellite image analysis and by the distribution of new ^{40}Ar – ^{39}Ar and Rb–Sr mica ages. At Meran the Southern Passeeier fault joins the Northern Passeeier fault, which outcrops for other 20 km towards the NNE of Meran. Together they form an over 40 km long, left-lateral transpressive fault system. The kinematics of the Southern Passeeier fault is inferred from the distribution of Oligocene radiometric ages to both sides of this fault, and this distribution is consistent with a 20 km left lateral displacement. A concomitant west-side up movement of less than 10 km is indicated by exhumation of the andalusite-bearing contact aureole of the Vigiljoch intrusion, which is cut off by the Southern Passeeier fault. ^{40}Ar – ^{39}Ar and Rb–Sr mica ages point to an emplacement of the Vigiljoch intrusion at 32 Ma, and suggest that the Southern Passeeier fault was active during late to post Oligocene time. The Passeeier fault belongs to the Periadriatic fault system and its activity is related to the indentation of the Southern Alps into the Austroalpine basement.

Keywords: Passeeier fault, Ar–Ar and Rb–Sr dating, satellite image analysis, contact aureole, Campo basement, Eastern Alps.

1. Introduction

A system of east- to southeast-dipping low angle normal faults (Fig. 1) accommodated a component of syn-compressional stretching within the Eastern Alps during the Late Cretaceous (FROITZHEIM, 1992; FROITZHEIM et al., 1994, 1997). A consequence of this extensional tectonic activity was the juxtaposition of the Campo basement against the Tonale basement (TB) along the Pejo detachment fault (PjF) (WERLING, 1992; MÜLLER, 1998; MÜLLER et al., in press). Late to post-Oligocene brittle-ductile overprinting of such Cretaceous exhumation structures occurred within the Austroalpine Meran-Mauls basement along sinistral transpressive faults belonging to the Periadriatic fault system (SPIESS, 1995; MÜLLER, 1998; VIOLA, 2000). In particular, along the steeply west dipping Northern

Passeeier fault (NPF), the western Meran-Mauls basement (WMMB) was juxtaposed against the eastern Meran-Mauls basement (EMMB). This resulted in an net jump of the Alpine radiometric age distribution (SPIESS, 1995), with Cretaceous ages prevailing to the west of the Northern Passeeier fault and pre-Alpine ages to the east.

We have now recognised a comparable fault within the Campo basement extending for at least 20 km from Meran toward the SSW. Although outcrops of this fault are limited to its northern sector, the full extent of the fault is revealed by the distribution of new radiometric mica ages presented here and can also be inferred from satellite image analysis. Because this fault influences the mica age distribution in a manner strikingly similar to the Northern Passeeier fault, we call it here the Southern Passeeier fault (SPF).

¹ Dipartimento di Mineralogia e Petrologia, Corso Garibaldi 37, I-35137 Padova, Italy. <richard@dmp.unipd.it>

² CNR – Centro di Studi per la Geodinamica Alpina, Corso Garibaldi 37, I-35137 Padova, Italy.

³ Institut für Geochronologie und Isotopengeochemie, GeoZentrum Wien, Althanstrasse 14, A-1090 Wien, Austria.

⁴ CNR-IRPI, Area di Ricerca, Corso Stati Uniti 4, I-35020 Padova, Italy.

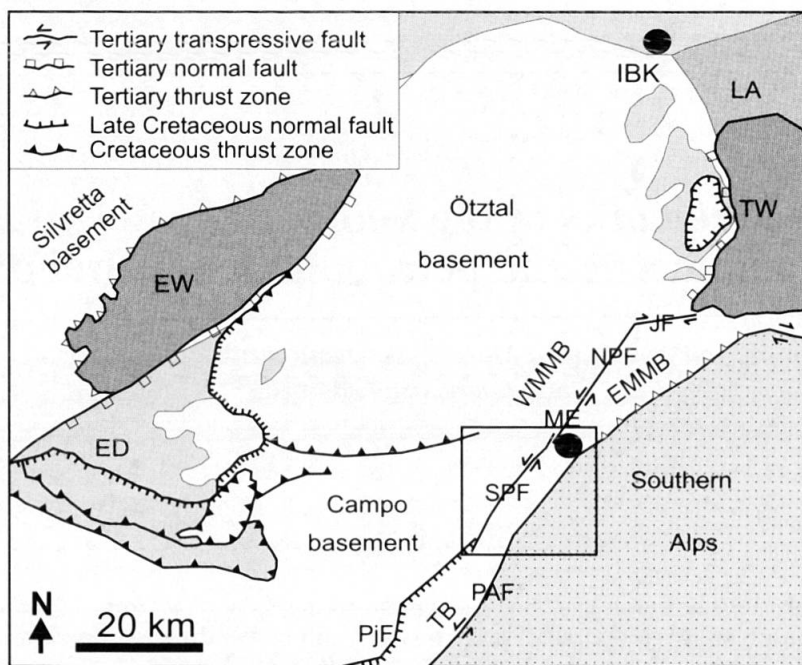


Fig. 1 Distribution of Cretaceous and Tertiary thrusts, normal faults and strike-slip faults in the Austroalpine basement between the Penninic Engadine window (EW) and Tauern window (TW). ED = Engadine dolomites, EMMB = eastern Meran-Mauls basement, IBK = Innsbruck, JF = Jaufen fault, LA = Lower Austroalpine, ME = Meran-Merano, NPF = Northern Passeier fault, PAF = Periadriatic fault, PjF = Pejo fault, SPF = Southern Passeier fault, TB = Tonale basement, WMMB = western Meran-Mauls basement. Rectangle shows the area investigated.

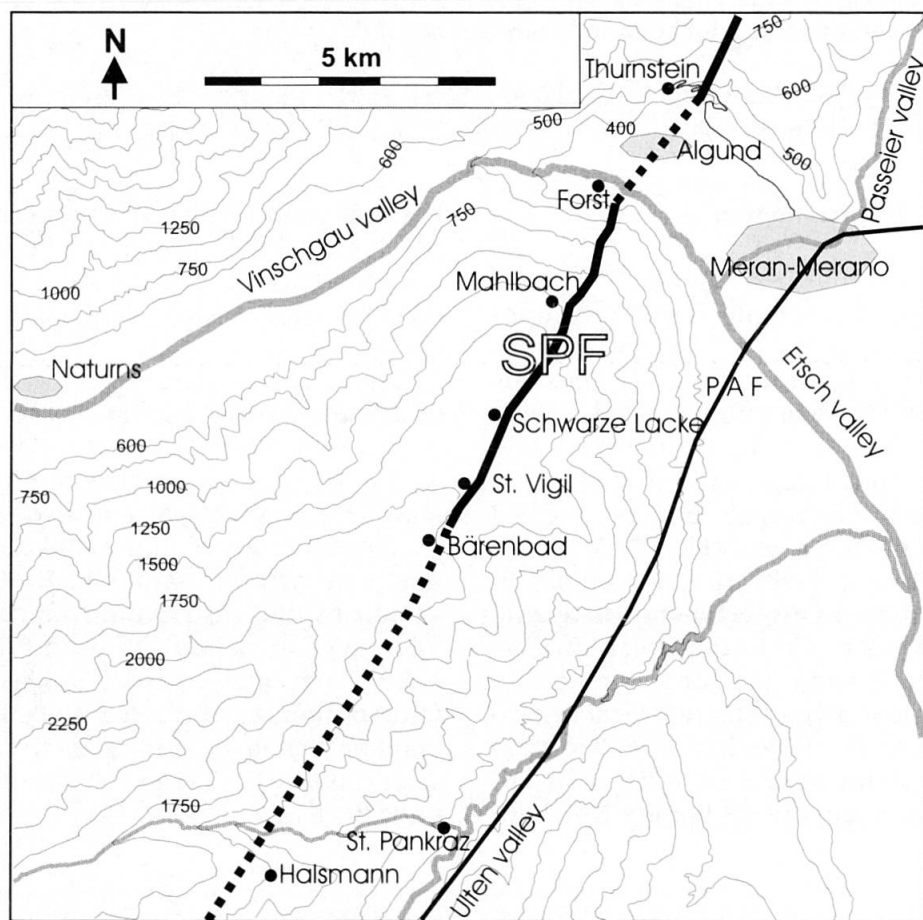


Fig. 2 Location of Southern Passeier fault (SPF). Continuous thick line shows the distribution of cataclastic to mylonitic rocks of the SPF in the field. Dotted line traces the SPF as recognised from the satellite image analysis and the radiometric age distribution pattern. The Periadriatic fault (PAF) is located to the east of the SPF.

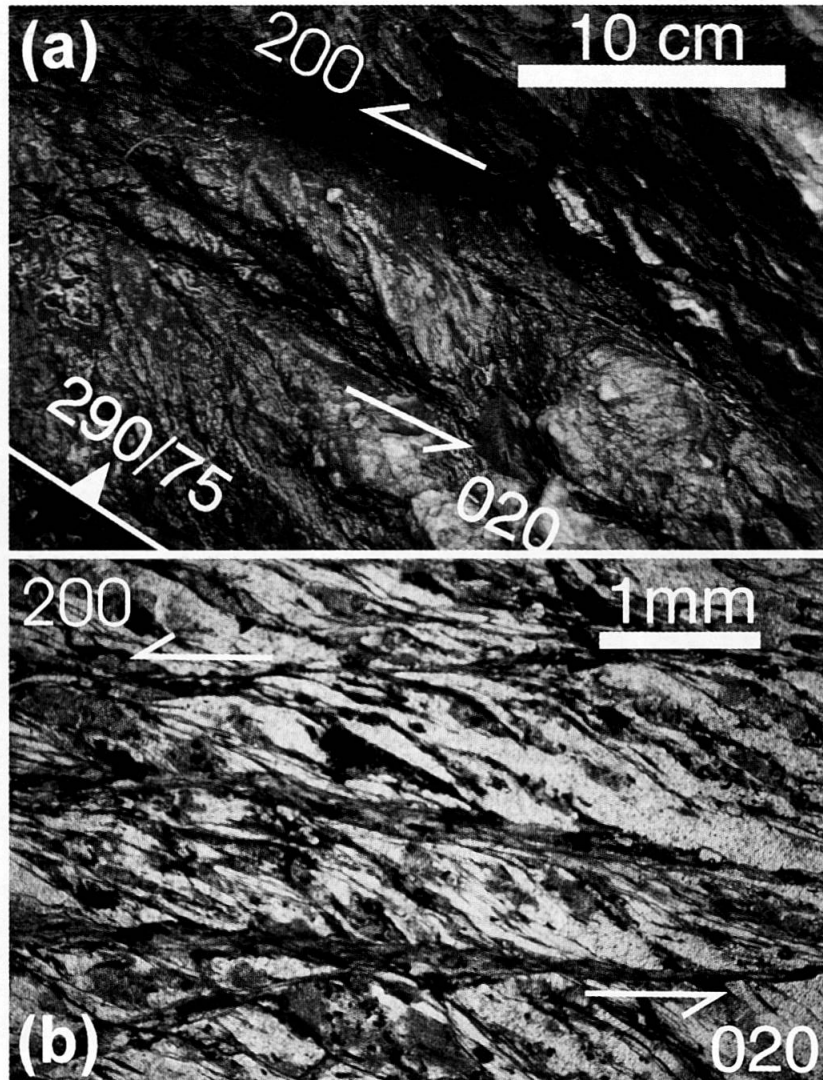


Fig. 3 Mylonite of the Southern Passeier fault. (a) Photograph of the outcrop at Forst-Marlinger Waalweg. The mylonitic foliation dips $290/75^\circ$ and the shear sense is sinistral. (b) Photomicrograph shows shear bands within the mylonite. Asymmetry of rotated foliation is consistent with a sinistral shear along the shear bands.

2. The Southern Passeier fault

2.1. EVIDENCE FROM THE FIELD

In the north of the investigated area, the Southern Passeier fault outcrops along the road from Meran to Thurnstein (Fig. 2). Its continuation to the south is first hidden by the thick alluvial fans and morainal deposits of the Etsch valley but can then be traced continuously from immediately east of Forst to Bärenbad (see figure 2 for location of localities). Cataclastic to mylonitic rocks of the Southern Passeier fault outcrop at Forst-Marlinger Waalweg (460 m above sea level, Figs 3a, b), Mahlbach-Mühlaler (1125 m), Schwarze Lacke (1730 m), St. Vigil (1800 m) and Bärenbad (1785 m).

2.2. EVIDENCE FROM SATELLITE IMAGE ANALYSES

SSW of Bärenbad, the Southern Passeier fault disappears under the morainal cover of the Vigiljoch area. To trace its continuation further toward the SSW we analysed a LANDSAT 5TM satellite image (Fig. 4) of the Vigiljoch area within the following Gauss-Boaga co-ordinates:

Upper left edge: X 5.654.130 m Y 1.172.160 m
Lower right edge: X 5.667.870 m Y 1.163.080 m

An iconographic reference frame has been obtained for the selected satellite image portion from analysis of the photographic infrared band 4 ($0.76\text{--}0.90 \mu\text{m}$ wavelength), which is particularly sensitive to vegetation differences. A stretching procedure transformed the icon obtained into a

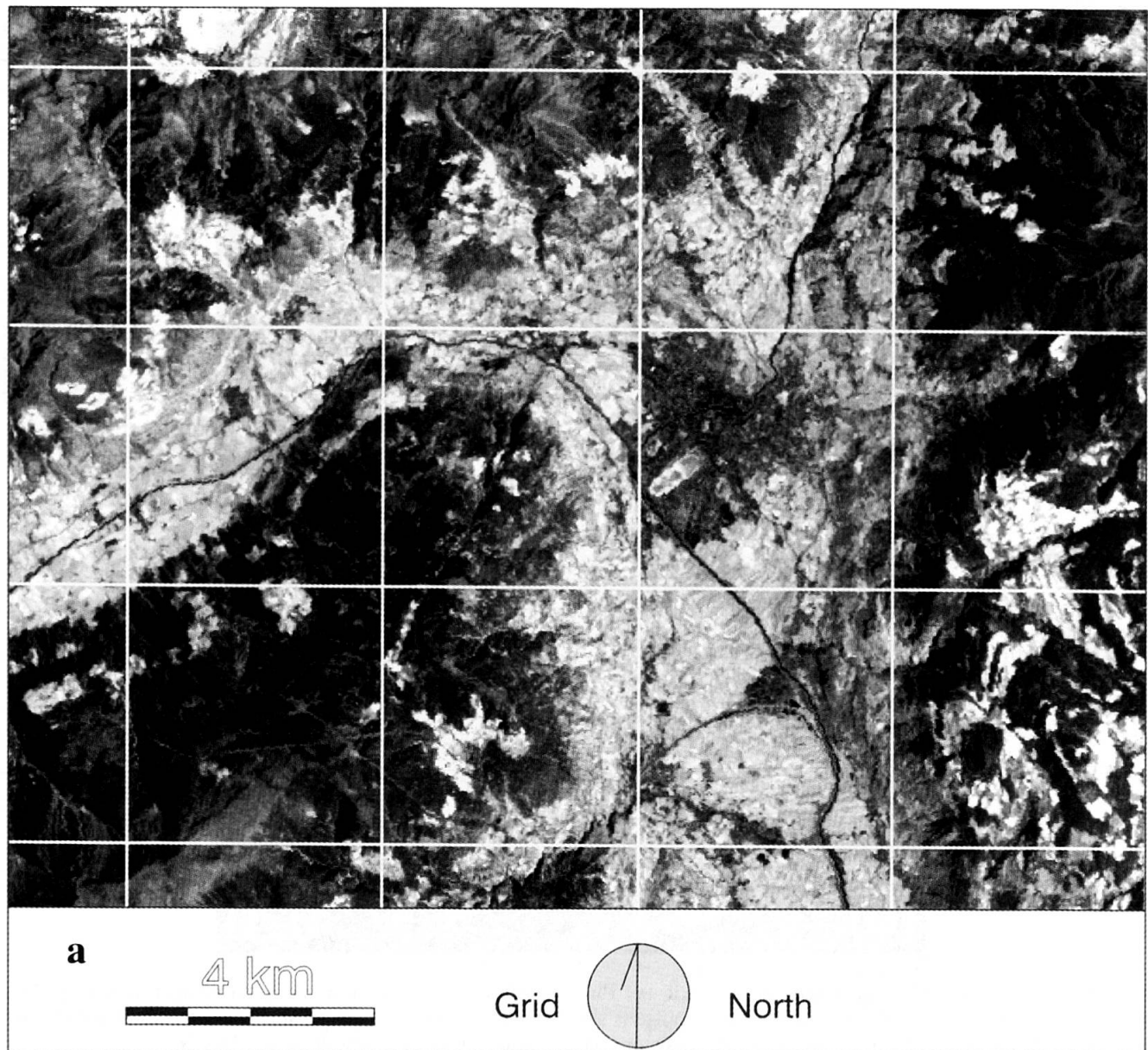


Fig. 4 LANDSAT 5TM satellite image of the Vigiljoch area showing the trace of the Southern Passeier fault. (a) grey level image obtained by the analysis of the photographic infrared band 4 (0.76–0.90 μm wavelength) using a stretching procedure. The continuous trace of the Southern Passeier fault can be easily recognised by a clearly visible chromatic variation (central part of the image). (b) the continuous white traces show the main linear features obtained by directional filtering of the photographic infrared band 4 in a SE–NW direction. NPF = Northern Passeier fault, PAF = Periadriatic fault, SPF = Souther Passeier fault.

256 grey level image, and directional filtering of the photographic infrared band 4 in a SE–NW direction allowed the main tectonic linear features of the area to be recognised, and in particular the continuous trace of the Southern Passeier fault (Figs 4a, b).

Figure 4a (compare with Fig. 4b) shows that the trace of the Southern Passeier fault (SPF), which runs approximately NNE–SSW, is unequivocally marked by a clearly discernible chromatic variation. We interpret this chromatic variation

and the related vegetation differences to reflect fluid circulation along the tectonic fault. Support for this comes from the distribution of the surface thermal anomalies calculated from thermal band 6 (10.4–12.5 μm wavelength) of the “Thematic Mapper” (TM). This distribution shows that the surface temperatures along the Southern Passeier fault is above the average, indicating warm water circulating upward along the Southern Passeier fault.

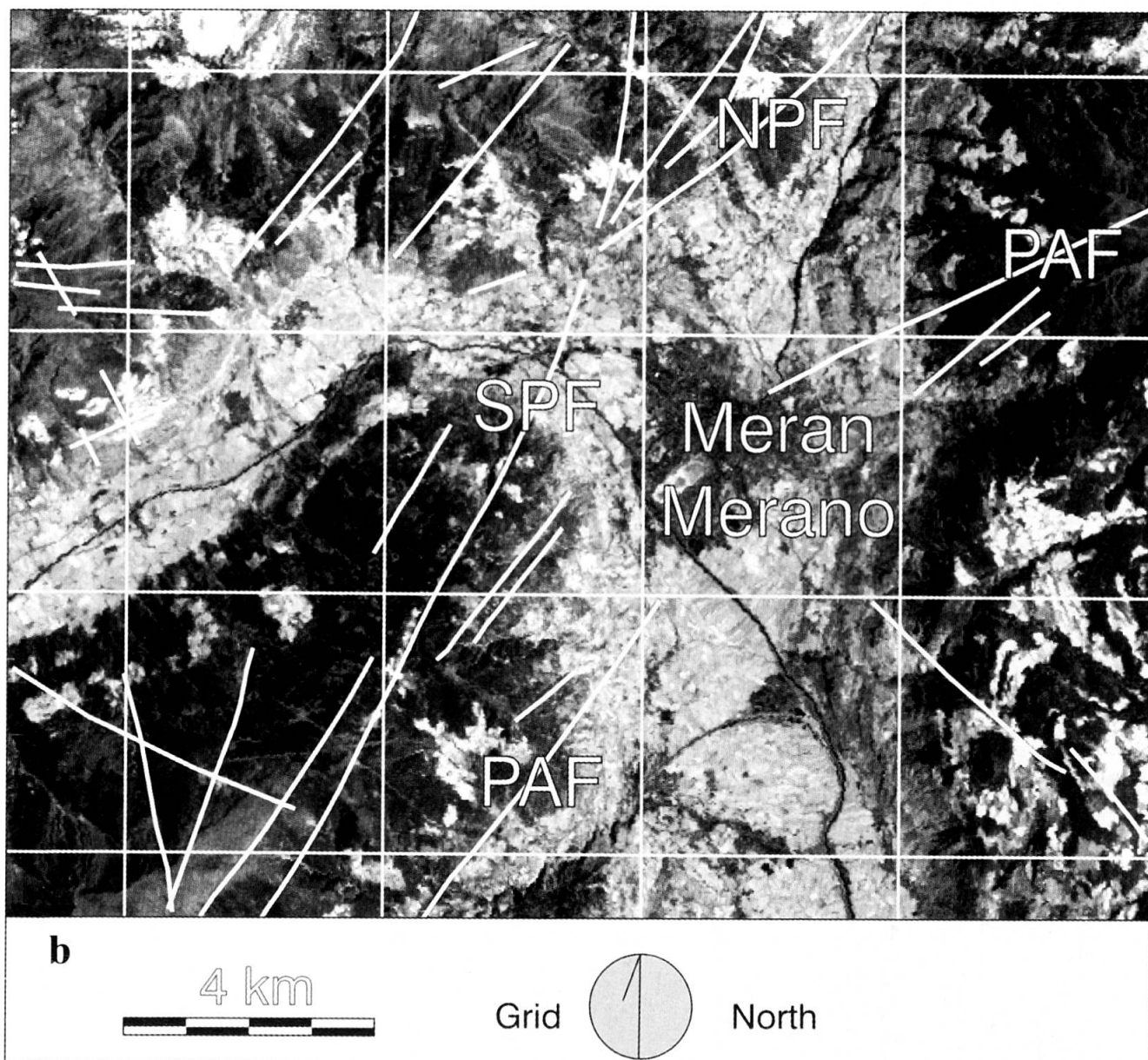


Fig. 4 (cont.)

3. Geochronology along the Southern Passeier fault

Fifteen mica-bearing rock samples were collected for geochronological investigation along the Southern Passeier fault. The sample locations are shown on figure 5 and in table 1. The micas of these samples were analysed for their ^{40}Ar - ^{39}Ar and Rb-Sr systematics, yielding a total of 24 new mica ages (see Appendix for details of analytical techniques).

3.1. ^{40}Ar - ^{39}Ar WHITE MICA AGES

White mica concentrates of 150–350 μm grain size were analysed from all 15 rock samples by the

^{40}Ar - ^{39}Ar stepwise-heating method. Ten steps between 650 and 1150 °C with single increments of 50 ± 5 °C were measured. A first-order analysis of the ages shows that they can be grouped into pre-Alpine (> 200 Ma) and Alpine (< 100 Ma) ages. Figure 5 shows that all Alpine ages are to the west of the Southern Passeier fault, whereas all pre-Alpine ages fall to the east of it. Consequently, there is a strong correlation between the mica age distribution and the strike of the Southern Passeier fault.

3.2. Rb-Sr BIOTITE AGES

Biotite concentrates of 150–350 μm grain size were analysed in 9 rock samples for their Rb-Sr systematics (white mica has not been analysed

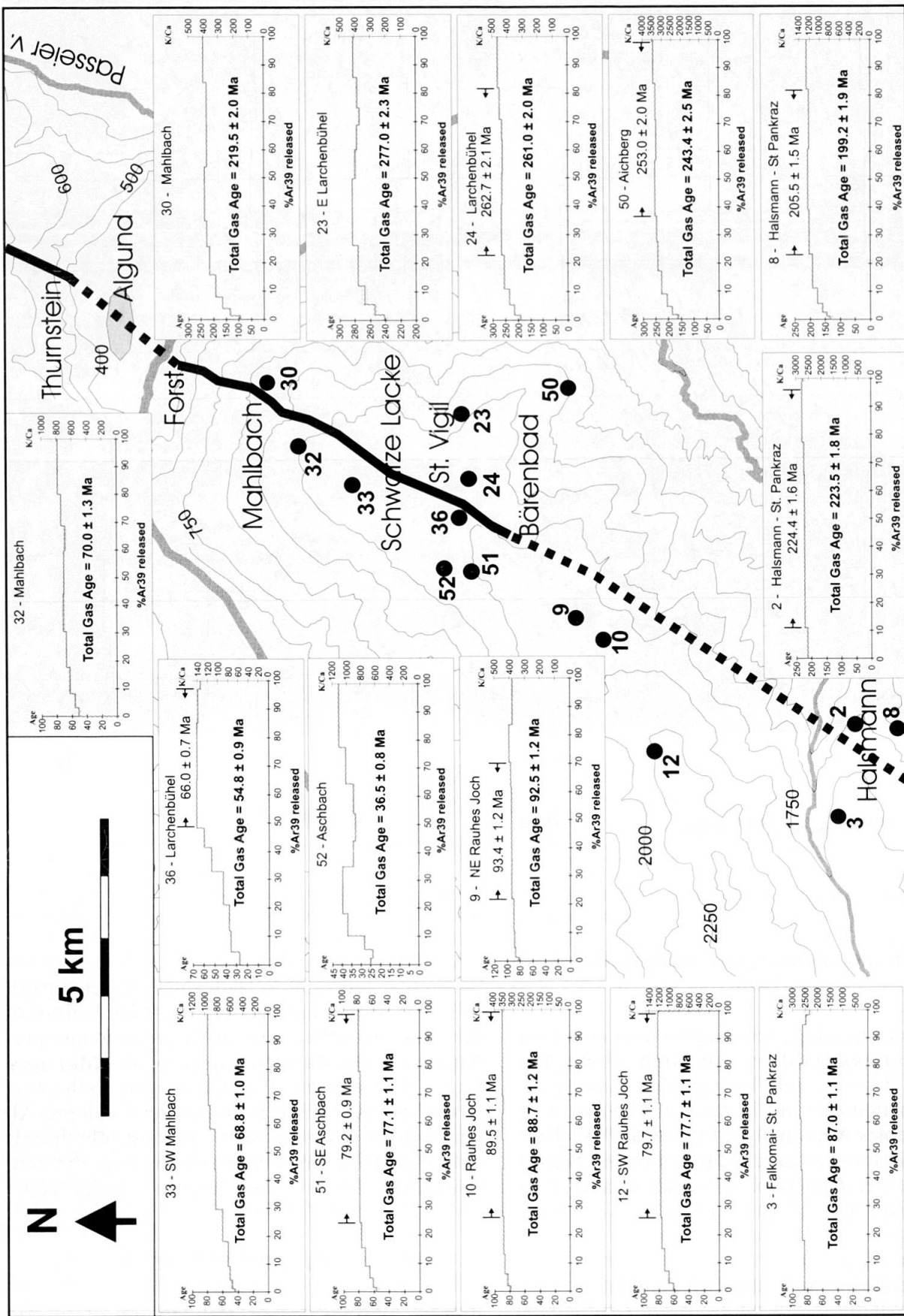


Fig. 5 ^{40}Ar - ^{39}Ar white mica age data. The figure shows sample locations (plus specimen numbers) and the different age spectra in relation to the trend of the Southern Passeier fault. To the west of this fault Alpine ages prevail, while to the east of it, Permo-Triassic ages dominate. On the western (Alpine) side, Oligocene ages occur in the north, which are related to a contact aureole.

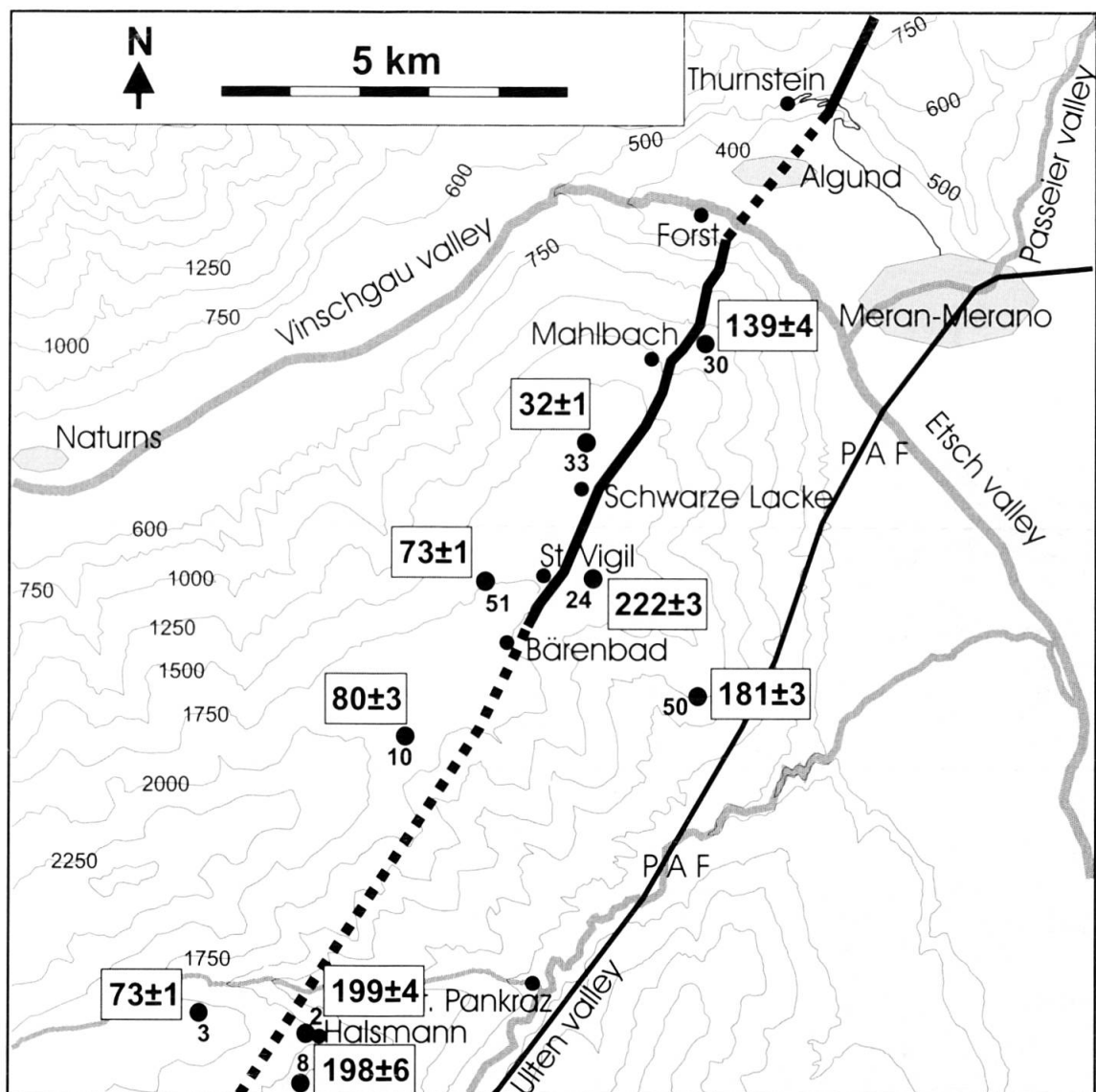


Fig. 6 Rb–Sr biotite ages. The figure shows the age data distribution in relation to the trend of the Southern Passeier fault. Alpine ages occur to the west of the fault. The Oligocene age of sample 33 relates to the contact aureole of the small Vigiljoch intrusive body. East of the fault, pre-Alpine ages prevail. Numbers adjacent to full dots are specimen numbers.

Tab. 1 Detailed sample location. Coordinates are shown according to the Universal Transverse Mercator (UTM) projection [for details see Istituto Geografico Militare Italiano (IGMI) maps indicated in the last column].

sample	rock type	UTM co-ordinates	locality	altitude (m)	IGMI map 1:50.000
2	mica schist	PS572608	Halsmann	1500	Appiano
3	mica schist	PS557613	Falkomai Alm	1725	Appiano
8	mica schist	PS568600	1.0 km SSW Halsmann	1400	Appiano
9	mica schist	PS587653	0.4 km ENE Rauhes Joch	1975	Merano
10	mica schist	PS583649	0.2 km SW Rauhes Joch	1975	Merano
12	mica schist	PS566640	2.0 km SW Rauhes Joch	2300	Merano
23	mica schist	PS617670	1.0 km E Larchenbühel	1400	Merano
24	mica schist	PS608670	Larchenbühel	1800	Merano
30	mica schist	PS621701	0.5 km E Mahlbach	1125	Merano
32	mica schist	PS612696	0.4 km SW Mahlbach	1450	Merano
33	gneiss	PS605686	1.5 km SW Mahlbach	1650	Merano
36	marble	PS603671	St. Vigil	1800	Merano
50	gneiss	PS622655	0.1 km S Aichberg	1300	Merano
51	mica schist	PS592669	1.0 km SSE Aschbach	1700	Merano
52	mica schist	PS594674	0.8 SE Aschbach	1650	Merano

Tab. 2 $^{40}\text{Ar}/^{39}\text{Ar}$ stepwise-heating isotopic data.

2 - Halsmann - St. Pankraz						
Date of measurement : 05/05/98						J = 0.005235 ± 0.4%
Date of irradiation : 15/02/98						
Sample weight: 4.1 mg						
Step	T[°C]	% ^{39}Ar	% $^{40}\text{Ar}_{\text{rad}}$	$^{39}\text{Ar}/^{37}\text{Ar}$	% $^{36}\text{Ca-Ar}$	$^{40}\text{Ar}_{\text{rad}}/^{39}\text{Ar}$
1	610	10.9 %	98.1 %	524	0.04 %	22.93 ± 0.5 %
2	655	21.5 %	99.0 %	1069	0.04 %	23.99 ± 0.1 %
3	710	21.2 %	99.2 %	1161	0.04 %	23.95 ± 0.4 %
4	770	11.7 %	98.8 %	1574	0.02 %	23.88 ± 0.8 %
5	820	11.9 %	98.9 %	2277	0.02 %	24.24 ± 0.5 %
6	865	17.4 %	99.5 %	2385	0.03 %	24.72 ± 0.1 %
7	920	4.3 %	98.0 %	1343	0.01 %	24.82 ± 0.9 %
8	1050	1.0 %	91.5 %	1085	0.00 %	24.42 ± 2.8 %
						total gas age: 223.5 ± 1.8
3 - Falkomai - St. Pankraz						
Date of measurement : 29/05/98						J = 0.005235 ± 0.4%
Date of irradiation : 12/02/98						
Sample weight: 4.1 mg						
Step	T[°C]	% ^{39}Ar	% $^{40}\text{Ar}_{\text{rad}}$	$^{39}\text{Ar}/^{37}\text{Ar}$	% $^{36}\text{Ca-Ar}$	$^{40}\text{Ar}_{\text{rad}}/^{39}\text{Ar}$
1	590	9.4 %	90.1 %	437	0.02 %	8.78 ± 0.7 %
2	610	8.4 %	91.6 %	646	0.02 %	8.72 ± 1.0 %
3	655	24.9 %	96.7 %	1130	0.03 %	9.02 ± 0.4 %
4	710	18.5 %	95.6 %	1508	0.01 %	9.17 ± 0.3 %
5	790	19.7 %	96.2 %	1943	0.01 %	9.34 ± 0.6 %
6	820	13.9 %	97.1 %	1534	0.02 %	8.99 ± 0.3 %
7	865	3.5 %	92.0 %	547	0.02 %	8.51 ± 1.9 %
8	980	1.7 %	85.0 %	816	0.01 %	7.99 ± 3.8 %
						total gas age: 87.0 ± 1.1
8 - Halsmann - St Pankraz						
Date of measurement : 05/06/98						J = 0.005235 ± 0.4%
Date of irradiation : 12/02/98						
Sample weight: 4.7 mg						
Step	T[°C]	% ^{39}Ar	% $^{40}\text{Ar}_{\text{rad}}$	$^{39}\text{Ar}/^{37}\text{Ar}$	% $^{36}\text{Ca-Ar}$	$^{40}\text{Ar}_{\text{rad}}/^{39}\text{Ar}$
1	590	1.3 %	88.3 %	37	0.13 %	14.08 ± 5.6 %
2	610	1.3 %	90.8 %	66	0.09 %	15.32 ± 1.8 %
3	655	3.1 %	93.2 %	65	0.12 %	16.78 ± 1.4 %
4	710	5.5 %	95.8 %	136	0.08 %	18.74 ± 0.9 %
5	770	12.1 %	97.5 %	272	0.06 %	20.52 ± 1.0 %
6	820	15.9 %	98.5 %	427	0.07 %	21.65 ± 0.3 %
7	865	21.8 %	99.1 %	485	0.10 %	22.08 ± 0.1 %
8	920	13.3 %	98.7 %	396	0.09 %	21.81 ± 0.5 %
9	980	8.0 %	98.2 %	204	0.11 %	21.79 ± 0.6 %
10	1070	17.7 %	98.9 %	770	0.05 %	22.49 ± 0.1 %
						total gas age: 199.2 ± 1.9

because of its significantly higher resetting temperature). All Rb-Sr ages are model ages and have been calculated using an assumed initial $^{87}\text{Sr}/^{86}\text{Sr}$ ratio of 0.71014 (see Appendix). A first-order analysis of the ages shows that the distribution of the pre-Alpine and Alpine Rb-Sr mica ages is also controlled by the strike of the Southern Passeier fault (Fig. 6).

3.3. TERTIARY CONTACT METAMORPHISM

Detailed analysis of the $^{40}\text{Ar}-^{39}\text{Ar}$ and Rb-Sr mica ages to the west of the Southern Passeier fault reveals that the ages become successively younger towards the NE, with samples 33 and 52 giving Oligocene ages near 32 Ma (compare Figs 5 and 6). While the Cretaceous ages in the SW reflect cooling after Eoalpine regional metamorphism, the young ages are related to an Oligocene

Tab. 2 (cont.)

9 - NE Rauhes Joch						
Date of measurement :	05/06/98					
Date of irradiation :	12/02/98					
Sample weight:	4.3 mg					
Step	T[°C]	% ^{39}Ar	% $^{40}\text{Ar}_{\text{rad}}$	$^{39}\text{Ar}/^{37}\text{Ar}$	% $^{36}\text{Ca-Ar}$	$^{40}\text{Ar}_{\text{rad}}/^{39}\text{Ar}$
1	610	1.4 %	80.4 %	42	0.10 %	8.53 ± 2.4 %
2	665	3.4 %	90.2 %	125	0.07 %	9.09 ± 1.5 %
3	715	5.9 %	93.9 %	184	0.09 %	9.18 ± 1.3 %
4	770	11.2 %	95.9 %	339	0.07 %	9.34 ± 0.8 %
5	815	14.9 %	96.9 %	448	0.07 %	9.64 ± 1.0 %
6	840	11.9 %	97.4 %	493	0.08 %	9.70 ± 0.6 %
7	890	13.0 %	96.9 %	339	0.09 %	9.70 ± 0.9 %
8	950	8.6 %	95.1 %	231	0.08 %	9.80 ± 0.5 %
9	1040	13.4 %	96.3 %	270	0.09 %	10.09 ± 0.6 %
10	1150	16.3 %	97.2 %	297	0.12 %	9.50 ± 0.5 %
						total gas age: 92.5 ± 1.2
10 - Rauhes Joch						
Date of measurement :	05/06/98					
Date of irradiation :	12/02/98					
Sample weight:	4.0 mg					
Step	T[°C]	% ^{39}Ar	% $^{40}\text{Ar}_{\text{rad}}$	$^{39}\text{Ar}/^{37}\text{Ar}$	% $^{36}\text{Ca-Ar}$	$^{40}\text{Ar}_{\text{rad}}/^{39}\text{Ar}$
1	610	1.8 %	79.8 %	48	0.09 %	8.22 ± 2.1 %
2	665	4.4 %	88.7 %	107	0.08 %	8.61 ± 1.8 %
3	715	7.0 %	92.9 %	167	0.08 %	8.96 ± 0.7 %
4	770	13.3 %	95.4 %	232	0.09 %	9.19 ± 0.8 %
5	815	17.0 %	96.2 %	295	0.09 %	9.29 ± 0.7 %
6	840	10.5 %	95.9 %	197	0.12 %	9.27 ± 0.7 %
7	890	9.2 %	94.6 %	245	0.07 %	9.34 ± 0.7 %
8	950	6.3 %	93.1 %	274	0.05 %	9.22 ± 1.4 %
9	1040	11.1 %	95.1 %	224	0.09 %	9.33 ± 0.8 %
10	1150	19.5 %	96.8 %	281	0.11 %	9.29 ± 0.2 %
						total gas age: 88.7 ± 1.2
12 - SW Rauhes Joch						
Date of measurement :	06/06/98					
Date of irradiation :	12/02/98					
Sample weight:	4.0 mg					
Step	T[°C]	% ^{39}Ar	% $^{40}\text{Ar}_{\text{rad}}$	$^{39}\text{Ar}/^{37}\text{Ar}$	% $^{36}\text{Ca-Ar}$	$^{40}\text{Ar}_{\text{rad}}/^{39}\text{Ar}$
2	665	2.7 %	79.1 %	70	0.08 %	6.29 ± 1.8 %
3	715	4.3 %	87.9 %	97	0.10 %	6.95 ± 1.5 %
4	770	8.1 %	93.1 %	309	0.06 %	7.51 ± 1.0 %
5	815	11.2 %	95.1 %	325	0.07 %	7.89 ± 0.6 %
6	840	12.0 %	96.9 %	466	0.08 %	8.08 ± 0.6 %
7	890	18.8 %	97.4 %	667	0.07 %	8.12 ± 1.2 %
8	950	10.2 %	96.3 %	582	0.05 %	8.17 ± 0.9 %
9	1040	15.5 %	97.2 %	968	0.04 %	8.32 ± 0.9 %
10	1150	17.2 %	98.4 %	1444	0.06 %	8.50 ± 0.7 %
						total gas age: 77.7 ± 1.1
23 - E - Larchenbüchel						
Date of measurement :	06/06/98					
Date of irradiation :	12/02/98					
Sample weight:	4.1 mg					
Step	T[°C]	% ^{39}Ar	% $^{40}\text{Ar}_{\text{rad}}$	$^{39}\text{Ar}/^{37}\text{Ar}$	% $^{36}\text{Ca-Ar}$	$^{40}\text{Ar}_{\text{rad}}/^{39}\text{Ar}$
1	610	1.9 %	91.8 %	68	0.06 %	26.10 ± 1.5 %
2	665	3.8 %	94.5 %	68	0.08 %	27.57 ± 1.0 %
3	715	6.4 %	96.6 %	165	0.05 %	29.11 ± 1.3 %
4	770	14.3 %	98.1 %	302	0.05 %	30.14 ± 0.2 %
5	815	23.4 %	99.1 %	500	0.07 %	30.98 ± 0.2 %
6	840	10.2 %	98.8 %	186	0.13 %	30.51 ± 0.6 %
7	890	8.7 %	98.7 %	320	0.07 %	30.32 ± 0.3 %
8	950	6.1 %	97.5 %	114	0.11 %	29.87 ± 0.4 %
9	1040	10.8 %	98.1 %	224	0.07 %	30.22 ± 0.5 %
10	1150	14.4 %	98.2 %	347	0.05 %	30.81 ± 0.3 %
						total gas age: 277.0 ± 2.3

Tab. 2 (cont.)

24 - Larchenbühel							
Date of measurement : 06/06/98 Date of irradiation : 12/02/98 Sample weight: 4.7 mg						J = 0.005235 ± 0.4%	
Step	T[°C]	% ^{39}Ar	% $^{40}\text{Ar}_{\text{rad}}$	$^{39}\text{Ar}/^{37}\text{Ar}$	% $^{36}\text{Ca-Ar}$	$^{40}\text{Ar}_{\text{rad}}/^{39}\text{Ar}$	age [Ma]
1	610	1.8 %	92.0 %	35	0.15 %	20.32 ± 1.3 %	190.6 ± 2.3
2	665	3.7 %	94.9 %	61	0.12 %	23.13 ± 0.5 %	215.4 ± 1.0
3	715	5.6 %	96.9 %	67	0.17 %	25.17 ± 0.5 %	233.3 ± 1.0
4	770	11.8 %	98.2 %	148	0.12 %	27.64 ± 0.2 %	254.8 ± 0.4
5	815	18.0 %	98.9 %	197	0.16 %	28.76 ± 0.4 %	264.3 ± 1.1
6	840	10.9 %	98.7 %	114	0.22 %	28.51 ± 0.3 %	262.3 ± 0.8
7	890	11.6 %	98.8 %	152	0.18 %	28.39 ± 0.3 %	261.2 ± 0.8
8	950	7.3 %	98.7 %	202	0.12 %	28.48 ± 0.5 %	262.0 ± 1.2
9	1040	11.2 %	98.6 %	111	0.20 %	29.49 ± 0.5 %	270.6 ± 1.3
10	1130	18.1 %	99.4 %	558	0.11 %	30.48 ± 0.2 %	279.1 ± 0.4
							total gas age: 261.0 ± 2.0
30 - Mahlbach							
Date of measurement : 06/06/98 Date of irradiation : 12/02/98 Sample weight: 5.8 mg						J = 0.004162 ± 0.4%	
Step	T[°C]	% ^{39}Ar	% $^{40}\text{Ar}_{\text{rad}}$	$^{39}\text{Ar}/^{37}\text{Ar}$	% $^{36}\text{Ca-Ar}$	$^{40}\text{Ar}_{\text{rad}}/^{39}\text{Ar}$	age [Ma]
1	610	1.3 %	69.0 %	33	0.05 %	12.60 ± 4.6 %	96.4 ± 4.3
2	665	2.7 %	86.7 %	54	0.06 %	17.70 ± 2.1 %	134.0 ± 2.7
3	715	3.9 %	93.1 %	69	0.08 %	21.99 ± 0.7 %	165.1 ± 1.1
4	770	8.0 %	96.1 %	132	0.07 %	25.66 ± 0.8 %	191.3 ± 1.5
5	815	9.9 %	97.3 %	193	0.06 %	29.17 ± 0.4 %	216.0 ± 0.8
6	848	9.0 %	97.6 %	189	0.06 %	30.70 ± 0.5 %	226.7 ± 1.0
7	890	19.2 %	98.8 %	349	0.07 %	31.75 ± 0.2 %	234.0 ± 0.5
8	950	15.9 %	98.4 %	317	0.06 %	30.50 ± 0.2 %	225.2 ± 0.4
9	1040	14.0 %	98.3 %	188	0.09 %	30.74 ± 0.6 %	227.0 ± 1.3
10	1130	16.1 %	98.6 %	231	0.09 %	32.54 ± 0.4 %	239.4 ± 0.8
							total gas age: 219.5 ± 2.0
32 - Mahlbach							
Date of measurement : 07/06/98 Date of irradiation : 12/02/98 Sample weight: 4.9 mg						J = 0.004162 ± 0.4%	
Step	T[°C]	% ^{39}Ar	% $^{40}\text{Ar}_{\text{rad}}$	$^{39}\text{Ar}/^{37}\text{Ar}$	% $^{36}\text{Ca-Ar}$	$^{40}\text{Ar}_{\text{rad}}/^{39}\text{Ar}$	age [Ma]
2	665	3.2 %	72.8 %	93	0.04 %	6.56 ± 4.0 %	50.8 ± 2.0
3	715	5.1 %	85.5 %	140	0.05 %	7.27 ± 1.9 %	56.2 ± 1.0
4	770	9.5 %	91.4 %	202	0.06 %	8.20 ± 1.5 %	63.2 ± 1.0
5	815	12.9 %	92.3 %	377	0.03 %	8.79 ± 0.7 %	67.8 ± 0.5
6	840	13.5 %	94.0 %	733	0.02 %	9.25 ± 1.8 %	71.2 ± 1.3
7	890	15.7 %	95.2 %	701	0.03 %	9.16 ± 0.7 %	70.6 ± 0.5
8	950	9.0 %	93.3 %	273	0.05 %	8.94 ± 2.1 %	68.8 ± 1.4
9	1040	11.3 %	92.8 %	221	0.06 %	9.64 ± 0.6 %	74.1 ± 0.4
10	1150	19.9 %	94.4 %	235	0.07 %	10.19 ± 0.3 %	78.3 ± 0.3
							total gas age: 70.0 ± 1.3
33 - SW Mahlbach							
Date of measurement : 07/06/98 Date of irradiation : 12/02/98 Sample weight: 4.4 mg						J = 0.004162 ± 0.4%	
Step	T[°C]	% ^{39}Ar	% $^{40}\text{Ar}_{\text{rad}}$	$^{39}\text{Ar}/^{37}\text{Ar}$	% $^{36}\text{Ca-Ar}$	$^{40}\text{Ar}_{\text{rad}}/^{39}\text{Ar}$	age [Ma]
1	610	1.3 %	71.4 %	124	0.03 %	5.69 ± 3.0 %	44.1 ± 1.3
2	665	3.1 %	80.7 %	217	0.03 %	6.19 ± 3.3 %	47.9 ± 1.5
3	715	4.7 %	86.8 %	348	0.03 %	6.58 ± 1.3 %	50.9 ± 0.6
4	770	9.0 %	89.7 %	384	0.03 %	6.85 ± 0.9 %	53.0 ± 0.5
5	815	11.6 %	90.3 %	485	0.02 %	7.85 ± 0.6 %	60.6 ± 0.4
6	840	14.3 %	94.1 %	1190	0.01 %	9.01 ± 0.5 %	69.4 ± 0.3
7	890	14.5 %	95.0 %	645	0.03 %	9.05 ± 0.5 %	69.7 ± 0.3
8	950	8.7 %	92.6 %	306	0.04 %	9.94 ± 1.3 %	76.4 ± 1.0
9	1040	10.8 %	91.3 %	210	0.04 %	10.27 ± 0.9 %	78.9 ± 0.7
10	1150	21.9 %	93.1 %	249	0.05 %	10.30 ± 0.2 %	79.1 ± 0.2
							total gas age: 68.8 ± 1.0

Tab. 2 (cont.)

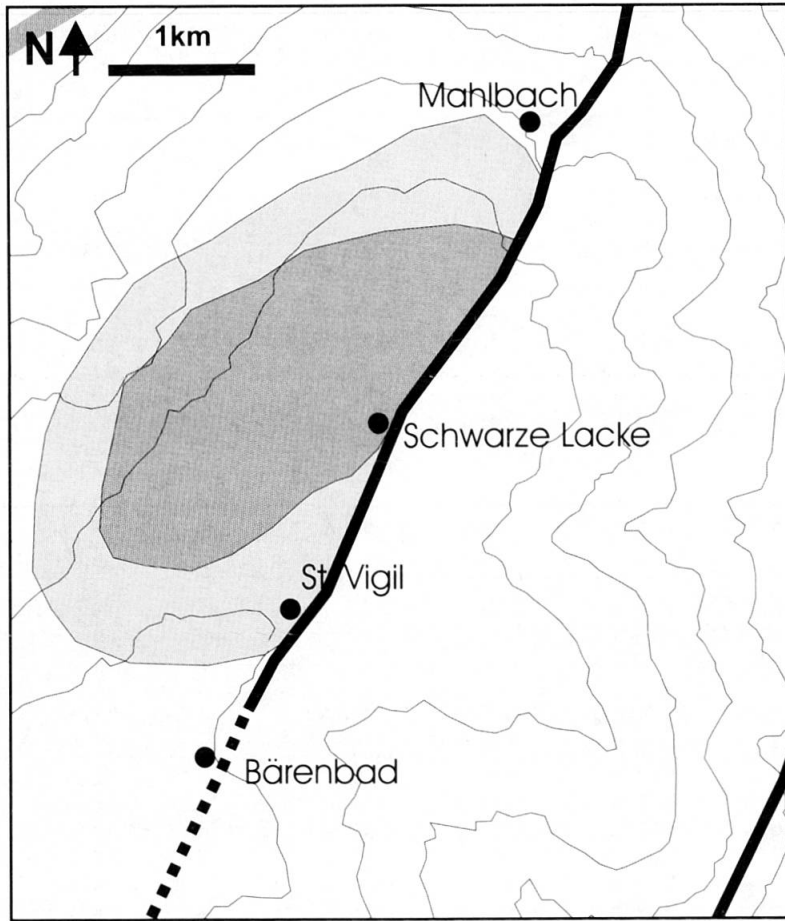
36 - Larchenbüchel						
				$J = 0.004162 \pm 0.4\%$		
Date of measurement : 07/06/98						
Date of irradiation : 12/02/98						
Sample weight: 4.6 mg						
Step	T[°C]	% ^{39}Ar	% $^{40}\text{Ar}_{\text{rad}}$	$^{39}\text{Ar}/^{37}\text{Ar}$	% $^{36}\text{Ca-Ar}$	$^{40}\text{Ar}_{\text{rad}}/^{39}\text{Ar}$
1	610	4.6 %	53.1 %	0	10.56 %	3.49 \pm 1.9 %
2	665	7.4 %	81.7 %	0	18.35 %	4.51 \pm 1.4 %
3	715	9.2 %	89.7 %	5	3.37 %	4.75 \pm 1.0 %
4	770	11.8 %	93.0 %	25	0.91 %	5.47 \pm 1.0 %
5	815	8.7 %	93.7 %	35	0.59 %	6.84 \pm 1.1 %
6	840	6.9 %	94.6 %	54	0.40 %	7.72 \pm 1.6 %
7	890	17.2 %	96.9 %	99	0.36 %	8.61 \pm 0.4 %
8	950	19.7 %	97.4 %	131	0.33 %	8.58 \pm 0.5 %
9	1040	11.8 %	97.2 %	90	0.46 %	8.46 \pm 0.9 %
10	1150	2.9 %	95.5 %	65	0.38 %	8.12 \pm 0.6 %
						total gas age: 54.8 \pm 0.9
50 - Aichberg						
Date of measurement : 07/06/98				$J = 0.004162 \pm 0.4\%$		
Date of irradiation : 12/02/98						
Sample weight: 4.7 mg						
Step	T[°C]	% ^{39}Ar	% $^{40}\text{Ar}_{\text{rad}}$	$^{39}\text{Ar}/^{37}\text{Ar}$	% $^{36}\text{Ca-Ar}$	$^{40}\text{Ar}_{\text{rad}}/^{39}\text{Ar}$
1	610	1.5 %	92.5 %	409	0.01 %	21.60 \pm 2.7 %
2	665	3.0 %	95.8 %	451	0.02 %	24.72 \pm 1.0 %
3	715	4.5 %	97.4 %	497	0.02 %	27.74 \pm 0.5 %
4	770	8.3 %	98.1 %	642	0.02 %	30.74 \pm 0.4 %
5	815	10.4 %	98.4 %	638	0.03 %	32.72 \pm 1.8 %
6	840	9.2 %	98.4 %	697	0.02 %	33.50 \pm 0.7 %
7	890	20.1 %	99.1 %	1915	0.02 %	34.55 \pm 0.2 %
8	950	14.4 %	99.0 %	2458	0.01 %	33.75 \pm 0.3 %
9	1040	13.2 %	98.8 %	1999	0.01 %	34.21 \pm 0.6 %
10	1130	15.6 %	99.0 %	2128	0.01 %	35.45 \pm 0.7 %
						total gas age: 243.4 \pm 2.5
51 - SE Aschbach						
Date of measurement : 08/06/98				$J = 0.004162 \pm 0.4\%$		
Date of irradiation : 12/02/98						
Sample weight: 4.0 mg						
Step	T[°C]	% ^{39}Ar	% $^{40}\text{Ar}_{\text{rad}}$	$^{39}\text{Ar}/^{37}\text{Ar}$	% $^{36}\text{Ca-Ar}$	$^{40}\text{Ar}_{\text{rad}}/^{39}\text{Ar}$
1	610	1.6 %	83.4 %	27	0.23 %	7.39 \pm 5.0 %
2	665	3.1 %	89.8 %	27	0.38 %	7.95 \pm 0.9 %
3	715	4.2 %	92.8 %	23	0.61 %	8.51 \pm 1.5 %
4	770	6.7 %	93.6 %	24	0.60 %	9.33 \pm 1.1 %
5	815	8.9 %	95.2 %	34	0.55 %	9.94 \pm 1.0 %
6	840	9.5 %	96.4 %	60	0.42 %	10.24 \pm 0.5 %
7	890	17.3 %	97.5 %	95	0.39 %	10.29 \pm 0.7 %
8	950	11.6 %	95.6 %	69	0.29 %	10.26 \pm 0.5 %
9	1040	15.2 %	95.7 %	67	0.31 %	10.20 \pm 0.5 %
10	1130	21.8 %	96.9 %	56	0.52 %	10.46 \pm 0.8 %
						total gas age: 77.0 \pm 1.1
52 - Aschbach						
Date of measurement : 22/06/98				$J = 0.004162 \pm 0.4\%$		
Date of irradiation : 12/02/98						
Sample weight: 10.7 mg						
Step	T[°C]	% ^{39}Ar	% $^{40}\text{Ar}_{\text{rad}}$	$^{39}\text{Ar}/^{37}\text{Ar}$	% $^{36}\text{Ca-Ar}$	$^{40}\text{Ar}_{\text{rad}}/^{39}\text{Ar}$
1	620	2.3 %	68.6 %	207	0.03 %	3.24 \pm 0.9 %
2	675	3.2 %	68.2 %	130	0.05 %	3.09 \pm 1.2 %
3	725	4.6 %	80.1 %	183	0.06 %	3.63 \pm 1.6 %
4	770	8.0 %	88.0 %	543	0.03 %	4.77 \pm 0.2 %
5	815	16.7 %	92.5 %	904	0.03 %	5.10 \pm 0.4 %
6	840	9.3 %	92.8 %	1278	0.02 %	4.40 \pm 0.9 %
7	800	9.6 %	92.9 %	976	0.03 %	4.23 \pm 1.4 %
8	950	10.7 %	91.0 %	1199	0.02 %	4.37 \pm 1.6 %
9	1065	12.8 %	86.7 %	634	0.02 %	4.88 \pm 0.6 %
10	1240	22.6 %	73.2 %	321	0.01 %	5.35 \pm 0.7 %
						total gas age: 36.5 \pm 0.8

Tab. 3 $^{87}\text{Sr}/^{87}\text{Sr}$ and $^{87}\text{Rb}/^{86}\text{Sr}$ ratios for analysed white mica concentrates.

sample	$^{87}\text{Rb}/^{86}\text{Sr}$	$^{87}\text{Sr}/^{86}\text{Sr}$	age (Ma)
2	166.57 ± 3.07	1.182500 ± 0.000160	199.49 ± 3.74
3	750.90 ± 12.11	1.488050 ± 0.000610	72.94 ± 1.23
8	111.51 ± 2.34	1.024500 ± 0.002500	198.38 ± 5.74
10	203.44 ± 5.09	0.940500 ± 0.003400	79.77 ± 3.17
24	151.13 ± 2.20	1.187180 ± 0.000320	221.99 ± 3.37
30	87.73 ± 1.92	0.883460 ± 0.000870	139.07 ± 3.73
33	332.98 ± 5.44	0.863670 ± 0.000350	32.47 ± 0.60
50	62.34 ± 0.91	0.870960 ± 0.000140	181.48 ± 2.80
51	83.84 ± 1.21	0.796597 ± 0.000035	72.60 ± 1.08

Tab. 4 Model age calculation for sample 51 using different Sr_i values. See appendix for discussion.

Sample	$^{87}\text{Rb}/^{86}\text{Sr}$	$^{87}\text{Sr}/^{86}\text{Sr}$	$^{87}\text{Sr}/^{86}\text{Sr}_i$	age (Ma)
51	83.84 ± 1.21	0.796597 ± 0.000035	0.70800	74.39 ± 1.10
51	83.84 ± 1.21	0.796597 ± 0.000035	0.71000	72.72 ± 1.08
51	83.84 ± 1.21	0.796597 ± 0.000035	0.71200	71.04 ± 1.05
51	83.84 ± 1.21	0.796597 ± 0.000035	0.71400	69.36 ± 1.03
51	83.84 ± 1.21	0.796597 ± 0.000035	0.71600	67.68 ± 1.01
51	83.84 ± 1.21	0.796597 ± 0.000035	0.71800	66.00 ± 0.98
51	83.84 ± 1.21	0.796597 ± 0.000035	0.72000	64.32 ± 0.96

Fig. 7 Contact aureole of the Vigiljoch intrusive body, which is truncated by the Southern Passeier fault (light grey $T > 350^\circ\text{C}$, dark grey $T > 450^\circ\text{C}$).

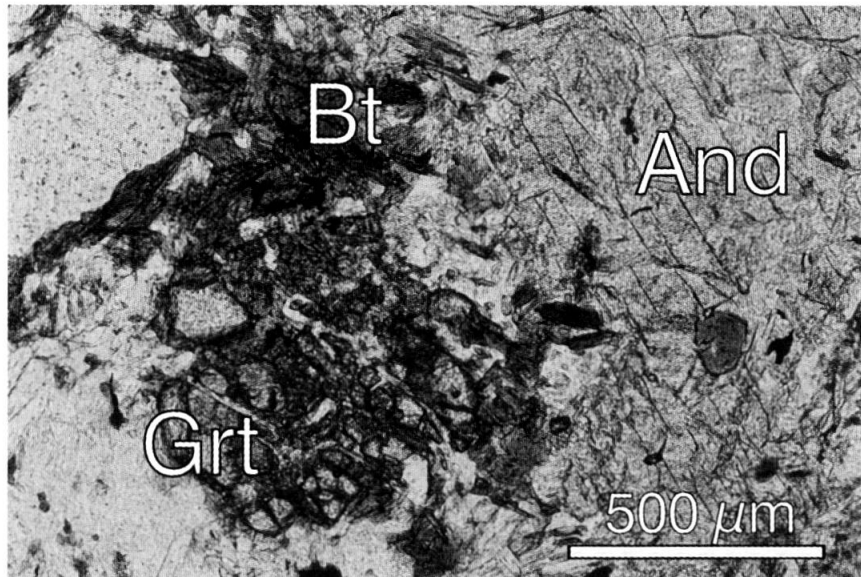


Fig. 8 Photomicrograph showing the mineral assemblage And + Bt + Grt + Ms + Qtz from the higher grade contact aureole around the Vigiljoch intrusion.

contact metamorphic aureole (Fig. 7). This aureole developed around an inferred small intrusive body located in the NE part of the Vigiljoch area. Although this intrusive body has not yet been exhumed, its contact aureole can be clearly mapped if thin sections are analysed. This has been done in this study, and samples 52 and 33 that belong to the higher grade part of this aureole (Fig. 7), show the contact metamorphic mineral assemblage And + Grt + Bt (Fig. 8). Samples 32, 36 and 51, which were taken from the lower grade part of the contact aureole (Fig. 7), show that large white mica flakes decompose statically into small muscovite crystals. The areal distribution of these transformations and of the Oligocene ages reveal that the contact aureole has been cut off by the Southern Passeier fault (Fig. 7). Within the Campo basement, comparable Oligocene intrusive bodies and numerous Oligocene dykes (DALPIAZ et al., 1988; MÜLLER et al., in press) are known from the “Grünsee” (upper Ultental valley) and the “Valle de la Mare” (to the N of Pejo), where micas from the contact aureole also give Oligocene K/Ar ages (THÖNI, 1981).

4. Discussion

The data presented here provide evidence for a scenario in which the Austroalpine Campo basement during the Cretaceous was first exhumed and cooled to below 300 °C, and was then further exhumed during the Oligocene along the left lateral, transpressive Southern Passeier fault. Several facts support this hypothesis.

(1) The evolution of a contact aureole of Oligocene age within a basement with Cretaceous mica ages requires that the basement had already cooled down during the Cretaceous to below the closure temperature for biotite in the Rb–Sr system (<300 °C). This cooling was aided by Cretaceous exhumation in response to detachment at a higher crustal level (Fig. 9a). The detached upper crustal level preserves evidence for a Permian to Triassic metamorphism (SPIESS et al., in prep.).

(2) Around 32 Ma ago several small magmatic bodies intruded into the Campo basement, with the formation of narrow contact aureoles (Fig. 9b).

(3) Along the left lateral Southern Passeier fault the Vigiljoch contact aureole was truncated sometime after 32 Ma, and concomitant with further exhumation of the Campo basement. A measure of the maximum west-side-up movement along the Southern Passeier fault is given by the stability of andalusite within the contact aureole, which suggests that the post-Oligocene exhumation was definitely less than 10 km (Fig. 9c).

In addition, our data potentially allow the magnitude of the left lateral strike slip component of the Passeier fault to be established. This is possible if the distribution of Oligocene ages within the basement situated to the east of the Passeier fault is considered. Within the eastern Meran-Mauls basement, such ages are only known from the Fartleis-Penserjoch area (FRANK et al., 1977; THÖNI, 1980; HAMMERSCHMIDT, 1982; SPIESS, 1991). Potentially these ages may reflect a higher than average heat flow due to the emplacement at depth of small Oligocene igneous bodies similar to those outcropping in the Campo basement

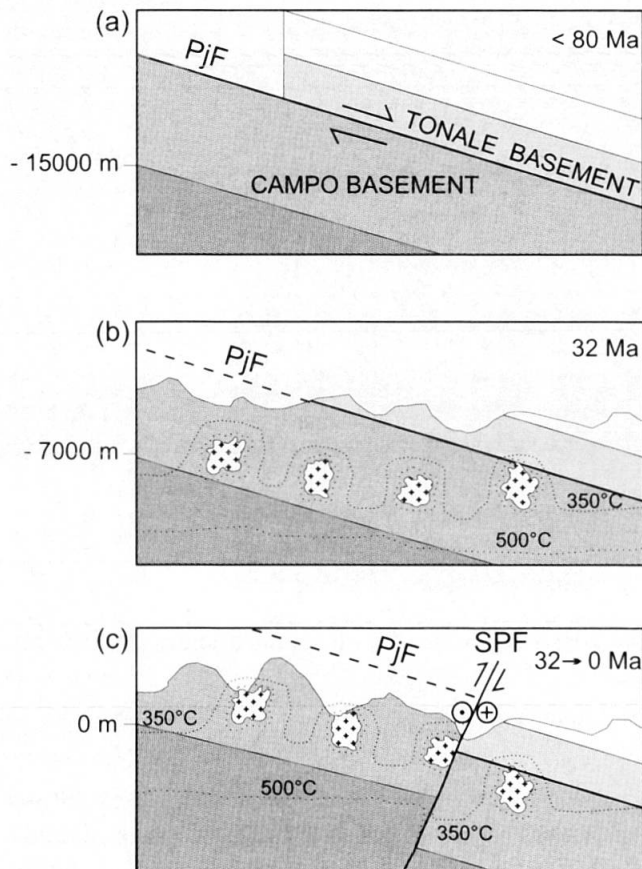


Fig. 9 Sketch showing the tectonic evolution of the Austroalpine Campo basement located to the west of the Southern Passeier fault, consistent with the age data and petrologic evidence. (a) Cretaceous exhumation of the Campo basement after detachment of the Tonale basement along the Pejo fault (PjF). (b) Intrusion of the Oligocene bodies in a basement, which had already cooled to below 300 °C during the Cretaceous and associated evolution of the contact aureoles around the intrusive bodies. (c) Truncation of the contact aureole of the Vigiljoch intrusion by left-lateral transpressive displacement along the Southern Passeier fault (SPF) sometime after intrusion. The Campo basement was exhumed by less than 10 km along this fault.

(Vigiljoch, Grünsee, Valle de la Mare). The higher than average heat flow along the Fartleis-Penserjoch area may also have facilitated the evolution of a several 100 meter thick mylonite zone (SPIESS, 1992) that developed here during the Oligocene. Therefore, if the Fartleis area before the Early Oligocene was aligned with the Vigiljoch area, then a left lateral transcurrent component of approximately 20 km results for the Passeier fault (Fig. 10). The inferred kinematics and the late to post Oligocene time of fault activity suggest that the Passeier fault has formed in response to the Tertiary indentation of the Southern Alps.

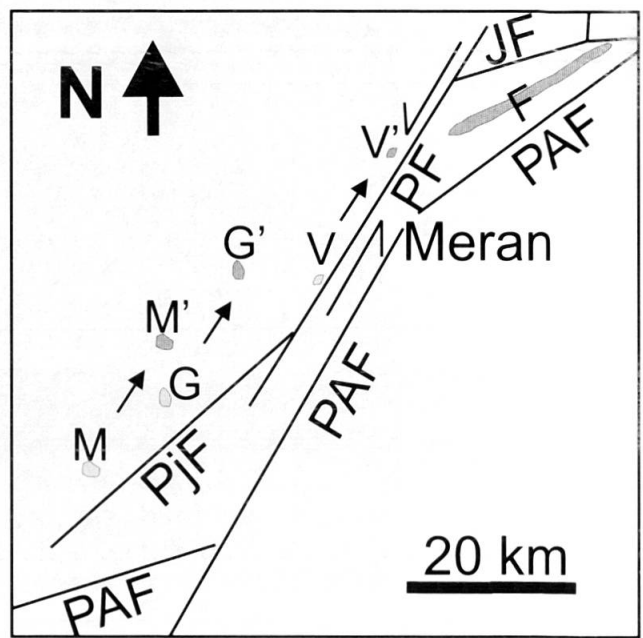


Fig. 10 Reconstruction of the left-lateral transcurrent component of the Passeier fault (PF). The actual position of the intrusive bodies of the Campo basement is shown by the light grey areas labelled M (Valle de la Mare), G (Grünsee) and V (Vigiljoch). Retro-movement of these Oligocene intrusive bodies (darker grey areas) for 20 km along PF to their respective positions M', G' and V' aligns them with the Fartleis-Penserjoch area (F), from which the only Oligocene ages of the eastern Meran-Mauls basement are known. No intrusive bodies outcrop in the Fartleis-Penserjoch area, but as in the Vigiljoch area they may not have been exhumed, and the associated heat budget is only reflected in the Oligocene mineral ages.

Acknowledgements

This research was funded by Italian MURST, University of Padova, CNR - Centro Studi per la Geodinamica Alpina - Padova. The critical review of Neil Mancktelow and Wolfgang Müller is very appreciated.

References

- DAL PIAZ, G. V., DEL MORO, A., MARTIN, S. and VENTURELLI, G. (1988): Post-collisional magmatism in the Ortler-Cevedale Massif (Northern Italy). *Jahrb. Geol. G.-A.*, 131, 533-551.
- FRANK, W., ALBER, J. and THÖNI, M. (1970): Jungalpine K/Ar-Alter von Hellelmmern aus aus dem Permo-Triaszug von Mauls/Penserjoch (Südtirol). *Anz. Österreich. Akad. Wiss., math.-naturwiss. Kl.* 7, 223-231.
- FRANK, W., KRALIK, M., SCHARBERT, S. and THÖNI M. (1987): Geochronological data from the Eastern Alps. In: FLÜGEL, H.W. and FAUPL, P. (eds): *Geodynamics of the Eastern Alps*, Deuticke Vienna, 272-275.
- FRIMMEL, H. E. and FRANK, W. (1997): Neoproterozoic tectono-thermal evolution of the Gariep Belt and its basement, Namibia and South Africa. *Prec. Research*, 90, 1-28.

- FROITZHEIM, N. (1992): Formation of recumbent folds during syn-orogenic crustal extension (Austroalpine nappes, Switzerland). *Geology*, 20, 923–926.
- FROITZHEIM, N., SCHMIDT, S.M. and CONTI, P. (1994): Repeated change from crustal shortening to orogen-parallel extension in the Austroalpine units of Graubünden. *Eclogae Geol. Helv.*, 87, 559–612.
- FROITZHEIM, N., CONTI, P. and DAALEN, VAN M. (1997): Late Cretaceous, synorogenic, low-angle normal faulting along the Schlinig fault (Switzerland, Italy, Austria) and its significance for the tectonics of the Eastern Alps. *Tectonophysics*, 280, 267–293.
- HAMMERSCHMIDT, K. (1982): K/Ar and 40Ar/39Ar age resolution from illites of the Trias of Mauls; Mesozoic cover of the Austroalpine basement, Eastern Alps (South Tyrol). *Schweiz. Mineral. Petrogr. Mitt.* 62, 113–133.
- MÜLLER, W. (1998): Isotopic dating of deformation using microsampling techniques: the evolution of the Periadriatic fault system. Ph.D. thesis n° 12580, ETH-Zürich, 135 pp.
- MÜLLER, W., PROSSER, G., MANCKTELOW, N.S., VILLA, I.M., KELLEY, S.P., VIOLA, G. and OBERLI, F. (2000): Geochronological constraints on the evolution of the Periadriatic Fault System (Alps). *International Journal of Earth Sciences*, in press.
- SPIESS, R. (1991): Petrographic evidence of fluid-controlled strain softening in an orthogneiss along a mylonitic zone St. Martin im Passerital-San Martino in Passiria (Eastern Alps). IGCP No. 276, Newsletter, 3, 475–477.
- SPIESS, R. (1992): Petrographisch-geologische und geochronologische Untersuchungen zur Bildung der Mylonitzone am Westende des Penserjochzuges. *Der Schlern*, 66, 95–104.
- SPIESS, R. (1995): The Passer-Jaufen Line: a tectonic boundary between the Variscan and the eo-Alpine Meran-Mauls basement. *Schweiz. Mineral. Petrogr. Mitt.*, 75, 413–425.
- THÖNI, M. (1980): Distribution of pre-Alpine and Alpine metamorphism of the Southern Ötztal Mass and the Scarl Unit, based on K/Ar age determinations. *Mitt. Österr. Geol. Ges.* 71/72, 139–165.
- THÖNI, M. (1981): Degree and Evolution of the Alpine Metamorphism in the Austroalpine Unit W of the Hohe Tauern in the light of K/Ar and Rb/Sr Age Determinations on Micas. *Jb. Geol. B.-A.*, 124, 111–174.
- WERLING, E. (1992): Tonale-, Pejo- und Judikarien-Linie: Kinematik, Mikrostrukturen und Metamorphose von Tektoniten aus räumlich interferierenden aber verschieden altrigen Verwerfungszenen. Ph.D. thesis, ETH-Zürich, 276 pp.
- VIOLA, G. (2000): Kinematics and timing of the Periadriatic fault system in the Giudicarie region (central-eastern Alps). Ph.D. thesis n° 13590, ETH-Zürich, 207 pp.

Manuscript received August 17, 2000; revision accepted May 1, 2001.

Appendix

ANALYTICAL TECHNIQUES

Mineral separation

After crushing, sieving and pre-concentration on a vibrating table, mica concentrates with primary grain sizes of up to 600 µm were ground in an agate mortar mill with alcohol to destroy mineral grains others than mica, to split up intergrown flakes and to remove inclusions of apatite etc. For normal samples, magnetic separation yields concentrates of typical purity around 99% or better. The after milling grain size of mica taken for analysis was 150–350 µm.

$^{40}\text{Ar}/^{39}\text{Ar}$ dating

A detailed insight into the analytical technique used is given in FRIMMEL and FRANK (1997), and only a summary is given here. Mineral concentrates were irradiated using the 9 MW ASTRA reactor at the Austrian Research Center, Seibersdorf. For Ar extraction, the RF-heating method is used. The heating period is 10 minutes for the low temperature steps and is continuously lowered to 3 minutes at the high temperature steps.

For the analysis of the cleaned gas, a VG-5400 mass spectrometer from FISONS ISOTOPES (Winsford, GB) was used (Vienna). Age calculation is done after correction for mass discrimination and radioactive decay, especially of the ^{37}Ar , using the formulas given in DALRYMPLE (1984).

J values are determined with an internal laboratory standard, calibrated against international standards. The errors given on the calculated age of an individual step include only the 1σ error of the analytical data. The error for the plateau ages or total gas ages includes an additional error of $\pm 0.4\%$ of the J-value. Within this error, the age results are reproducible with the same analytical equipment. Interlaboratory reproducibility can be expected within 1–1.5%. Table 2 shows the analytical results of the measured white micas.

Rb–Sr dating

The isotope dilution method (ID) was used for all Rb/Sr analyses and all $^{87}\text{Sr}/^{86}\text{Sr}$ -ratios have been calculated from ID analyses (Tab. 3). All Rb and Sr measurements were made on a VG ISOMASS

54E mass spectrometer (CNR-Padova). The measured mean $^{87}\text{Sr}/^{86}\text{Sr}$ -ratio for the NBS987 Sr-standard is 0.71018 ± 2 . The blank for the whole chemical treatment is < 2 ng Sr. All Rb-Sr model ages were calculated using an assumed initial $^{87}\text{Sr}/^{86}\text{Sr}$ ratio of 0.71014, and the constants of STEIGER and JÄGER (1977) were used for age calculations. The error values reported for the Rb-Sr ages were calculated by combining the error of the $^{87}\text{Sr}/^{86}\text{Sr}$ ratio with that of the $^{87}\text{Rb}/^{86}\text{Sr}$ ratio in the most unfavourable way. The error of the $^{87}\text{Rb}/^{86}\text{Sr}$ ratio is usually about 1.5%.

For the calculation of the model ages, we have used the initial $^{87}\text{Sr}/^{86}\text{Sr}$ ratio of 0.71014. For the aim of our research, which is distinguishing Alpine from pre-Alpine ages, this approach is justified, considered that the potential error that will be introduced is small compared to the age difference to be resolved. In fact, considering the standard model age formula, it results that the ages of those mica concentrates which have their measured $^{87}\text{Sr}/^{86}\text{Sr}$ -ratios closest to the Sr_i values

(0.71014 assumed in our calculation) will be affected by the largest errors. In our case the biotite with the lowest measured $^{87}\text{Sr}/^{86}\text{Sr}$ -ratio is sample 51, with a $^{87}\text{Sr}/^{86}\text{Sr}$ -ratio of 0.796597. All other samples have substantially higher $^{87}\text{Sr}/^{86}\text{Sr}$ ratios. We have calculated the variation of model ages for sample 51, for Sr_i values ranging from 0.708 to 0.720. In this interval fall most of the $^{87}\text{Sr}/^{86}\text{Sr}$ -ratios of paragneisses and micaschists of the Eastern Alps, and typical values are between 0.710–0.714 (FRANK et al., 1987). Table 4 shows that the calculated ages for sample 51 vary from 74 Ma ($\text{Sr}_i = 0.708$) to 64 Ma ($\text{Sr}_i = 0.720$). This age difference means that an error of more than ~ 8 Ma is unreasonable, and that the likely error for sample 51 (calculated model age = 72 Ma with $\text{Sr}_i = 0.71014$) is 3 Ma. Considered that the measured $^{87}\text{Sr}/^{86}\text{Sr}$ ratios of all other mica concentrates are significantly higher than that of sample 51 (Tab. 3), their model ages should be affected by a maximum error of less than ± 5 Ma.